

PRE-PRINT (BEFORE PEER REVIEW)

To access the post-print version:

Acta Materialia, 2014. Vol **68**: p. 150-158

[doi:10.1016/j.actamat.2014.01.018](https://doi.org/10.1016/j.actamat.2014.01.018)

Title: Microstructure and mechanical properties of a novel β titanium metallic composite by Selective Laser Melting.

Authors: Vrancken B.¹, Thijs L.¹, Kruth J.-P.², Van Humbeeck J.¹

¹ *University of Leuven, Department of Metallurgy and Materials Engineering, Belgium*

² *University of Leuven, Department of Mechanical Engineering, Belgium*

bey.vrancken@mtm.kuleuven.be (corresponding author)

lore.thijs@mtm.kuleuven.be

jean-pierre.kruth@mech.kuleuven.be

jan.vanhumbeeck@mtm.kuleuven.be

Please send all correspondence to the following author:

Bey Vrancken

Department of Metallurgy and Materials Engineering (MTM)

Kasteelpark Arenberg 44 - box 2450

3001 Leuven

Belgium

Tel: +32 16 321286

Fax: +32 16 321992

e-mail: bey.vrancken@mtm.kuleuven.be

Abstract

Selective Laser Melting is an Additive Manufacturing process in which functional, complex parts are produced by selectively melting consecutive layers of powder with a laser beam. This flexibility enables the exploration of a wide spectrum of possibilities in creating novel alloys or even metal-metal composites with unique microstructures. In this research, Ti6Al4V-ELI powder was mixed with 10 wt% Mo powder. In contrast to the fully α' microstructure of Ti6Al4V after SLM, the novel microstructure consists of a β titanium matrix with randomly dispersed pure Mo particles, as observed by light optical microscopy, scanning electron microscopy (SEM) and X-ray diffraction (XRD). Most importantly, the solidification mechanism changes from planar to cellular mode. Microstructures after heat treatment indicate the β phase is metastable and locate the β transus around 900°C, and tensile properties are equal to or better than conventional β titanium alloys.

Keywords: Selective Laser Melting, Additive Manufacturing, Ti6Al4V, β Titanium alloys, Solidification.

1. Introduction

In Selective Laser Melting (SLM) a high power laser locally melts successive layers of powder to produce complex shape 3D metal parts. The highly localized heat input leads to fast melting and solidification, resulting in a unique microstructure. SLM possesses several advantages over other production techniques, such as a high material use efficiency, a high level of flexibility and near net shape production of geometrically complex structural parts. The process details and applications have been widely reviewed elsewhere. For example, the reader is referred to Ref [1] for more details.

Titanium alloys are among the most widely used alloys in SLM due to their high specific strength and excellent biocompatibility. A lot of research effort has thus been focused on the influence of process parameters on the microstructure and related mechanical properties of titanium parts produced by SLM. For example, literature reports on SLM of pure Ti [2], Ti6Al7Nb [3], Nitinol [4, 5], other β titanium alloys [6], and most importantly, Ti6Al4V [7-12]. Concerning the latter, all authors report a microstructure consisting of martensitic α' within columnar prior β grains, the orientation of which depends on the scanning strategy.

Combining different powders and processing the mixture via SLM opens up a whole new and exciting research field. Hua *et al.* [13] combined elemental powder of Ti, Al and V to produce a bulk Ti6Al4V part. All three elements were mixed homogeneously in the melt and mechanical properties were found to be at least equal to those of parts produced with prealloyed powder. Several authors [14-18] have reported on the production of several types of in-situ metal matrix composites (MMCs), including different titanium matrix composites. More specifically, Collins *et al.* [19] were the first to mix Ti and Mo powder via Additive Manufacturing, using laser cladding. By creating compositionally graded structures, the microstructure and hardness for varying Mo content was examined, concluding that the highest hardness of 450 HV is reached by adding 15 wt% Mo. Recently, Almeida *et al.* [20] also used laser cladding and performed tensile tests on parts with different Mo content.

The optimal combination of a low Young's modulus (75 GPa) and adequate hardness (240 HV) was obtained by adding 13 wt% Mo.

In this paper, the solidification, microstructure, mechanical properties and response to heat treatment of SLM parts produced using a mixture of Ti6Al4V-ELI powder with 10 wt% Mo powder is described. Throughout the text, the novel material will be compared with regular Ti6Al4V-ELI processed by SLM under the exact same conditions. From here on, the '-ELI' suffix will be dropped.

2. Materials and Methods

Extra-low interstitial Ti6Al4V (Grade 23) powder was used as a base material for the SLM process. The powder is produced via the plasma-atomization process. The particle size ranges from 5 to 50 μm , with a d_{50} of 34 μm . The Mo powder particles are irregular and small compared to the Ti6Al4V powder, as shown in Figure 1, with an average size between 5 and 10 μm .

All samples were produced on the in-house developed LM-Q machine of the PMA Division of the department of mechanical engineering, KU Leuven. More details on this machine can be found in Ref. [21]. Samples were produced using a scanning speed v of 1600 mm/s, a laser power P of 250 W, 60 μm hatch spacing h , and a 30 μm layer thickness t . Layers were scanned using a continuous laser mode according to a zigzag pattern, rotated 90° between each layer. These parameters were previously optimized to obtain fully dense, good quality Ti6Al4V products [12, 22].

The exact amount of Mo in the parts was determined by inductively coupled plasma atomic emission spectroscopy (ICP-AES). HNO_3 was added after dissolving the majority of the sample in HCl to dissolve leftover Mo. The average composition was determined to be 5.89 wt% Al, 3.35 wt% V and 10.5 wt% Mo, remainder Ti.

Before microstructural examination, samples were ground using a SiC grinding paper with fine 1200 grit sizes, and polished using a $\text{SiO}_2\text{-H}_2\text{O}_2$ solution. To reveal the microstructure, an etchant containing 50 ml distilled water, 25 ml HNO_3 and 5 ml HF was used. Microstructural study was

performed on an Axioskop 40 Pol/40 A Pol microscope. A Philips SEM XL30 FEG was used for the examination of fracture surfaces and higher resolution micrographs. Texture and crystallographic orientation were examined by X-ray diffraction (XRD). A Siemens D500 diffractometer with Cu radiation with a wavelength of 1.54184 Å was used for X-ray diffraction. Pole figures for the β phase were measured using the (110) reflections at a diffraction angle 2θ of 39.2°, (200) at 56.9°, (211) at 71.2° and (310) at 97.6°. X-ray measurements were performed on polished cross sections perpendicular to the building direction.

Vickers microhardness tests were performed on a Leitz-Durimet microhardness tester using a weight of 300 g.

Heat treatments were performed in a vertical tube furnace under pure argon atmosphere with a heating rate of 10°C/min, 30 minute residence time and subsequent water quench with a delay of less than 1 second.

Four tensile test samples were built as rectangular beams from which the final shape was milled. Tensile tests were performed according to ASTM E 8M at a strain rate of 1 mm/min. Yield stress and Young's modulus were determined according to ASTM E 111. Tensile test loading direction was perpendicular to the building direction.

Charpy V-notch samples were built with the long axis parallel (vertically) and perpendicular (horizontally) to the building direction. The notch was included in the design instead of EDM'ed afterwards, as this reduces labor time and does not have a significant effect on the results [23]. Charpy V-notch impact testing was performed using an Instron Wolpert PW5. Specimen dimensions were those of the standard sub-size specimen as defined in ASTM Standard E23.

Thermodynamic calculations of the Ti-Al-V-Mo system were performed using the ThermoCalc software and the commercially available TCFE7 database.

3. Results

3.1 Microstructure

Figure 2a shows a side view cross section of the macrostructure of Ti6Al4V processed via SLM. The characteristic columnar prior β grains extend over multiple layers, up to several millimeters long. These columnar grains arise due to partial remelting of previously consolidated layers, allowing epitaxial growth. Combined with the stability of the planar solidification front, large columnar grains are formed. By contrast, no columnar β grains are detected after the addition of 10wt% Mo to the Ti6Al4V, as shown in Figure 2b. In this side view, the melt pool shape is revealed by local concentration variations of Mo in the material. Unmolten Mo particles are randomly distributed in the β titanium matrix and are present in various sizes but are generally smaller than 10 μm . These particles are indicated by the white arrows in Figure 2b and are clearer in Figure 3. The volume fraction of remaining Mo particles was calculated via pixelcount of SEM images taken with BSE contrast, such as Figure 3. In these images, the Mo particles are lighter than the surrounding matrix due to the larger atomic number of Mo compared to Ti. At 0,8%, the Mo particle content is too low to be measured via XRD and no Mo peaks are present in the diffraction spectra discussed below and shown in Figure 6.

The Mo particles are distributed homogeneously in the matrix, as indicated by the white arrows in Figure 2b. Furthermore, the local variations in color of the matrix, visible in Figure 3, indicate Mo rich and Mo poor bands due to an incomplete mixing of Mo in the melt pool or diffusion of Mo around the Mo particles. Mo is known to have a low diffusivity in the solid β -Ti phase of $0.3 \times 10^{-9} \text{ cm}^2/\text{s}$ at 1000°C [24] and thus it is likely that the diffusivity in the liquid phase is also comparatively low. The lighter bands are richer in Mo, and the bands outline the elliptical shape of the melt pool, as shown in Figure 3. This is a further indication that solidification during SLM happens in extremely short time periods.

On a microscopic scale, acicular martensitic α' is formed inside the prior β grains of Ti6Al4V due to the high cooling rates during SLM. The Burgers relation given in Equation (1) describes the

crystallographic relation between the α phase and the β phase from which it is formed. Perpendicular variants of the Burgers relation lead to the meshed pattern of α' needles within a prior β grain, visible in Figure 2a. The rapid solidification and martensitic microstructure lead to a Vickers microhardness of $399 \pm 5 \text{ HV}_{0.3;10s}$.

$$\begin{aligned} (110)_{\beta} &\leftrightarrow (0001)_{\alpha} \\ \langle 1\bar{1}1 \rangle_{\beta} &\leftrightarrow \langle 11\bar{2}0 \rangle_{\alpha} \end{aligned} \quad (1)$$

Figure 4 on the other hand shows the smaller β grains of the material with 10 wt% Mo. The melt pool boundaries are prominently delineated and may act as nucleation sites for new grains. However, most grains grow epitaxially across the melt pool boundaries, indicated by the white arrows, and form elongated grains. These grains grow towards the top center of the melt pool, in the opposite direction of the maximum thermal gradient. Contrary to Ti6Al4V, the melt pool boundary is still visible. The grains are typically 5 to 15 μm wide, which is much smaller than the columnar grains in Ti6Al4V, which range from 50 to 150 μm in width. Within each grain, a cellular substructure with an intercellular spacing of less than 1 μm is present, also directed towards the top melt pool center. This substructure within each grain is characteristic of welds and has recently also been reported for numerous materials processed via SLM [25]. In fact, an almost identical microstructure was described in detail for SLM of AlSi10Mg [26]. The prevalence of the β phase rather than the α' phase leads to a slightly lower hardness of $338 \pm 5 \text{ HV}_{0.3;10s}$, compared to $399 \text{ HV}_{0.3;10s}$ for Ti6Al4V. Combined with the results above, microsegregation of alloying elements occurs at two different scales. On the larger scale, Mo bands delineate the melt pool shape. On the smaller scale, Mo, Al and V are segregated due to the formation of the cellular solidification structure.

In a review of Ti-Mo alloys, Murray [27] summarized results from several independent studies stating that the β transus temperature lowers around 9 to 10°C per wt% Mo added. Given that the β transus of Ti6Al4V is 995°C, the new β transus is expected to be around 900°C. To examine the stability of the

β phase and validate this assumption, four samples were respectively subjected to an annealing temperature of 650°C, 850°C, 900°C and 1050°C for 30 minutes, followed by water quenching.

Microstructural examination showed that the sample treated at 650°C contained an extremely fine distribution of needle or plate like α , as shown in Figure 5a. XRD diffraction confirmed that α phase was present, as clear α peaks appear in the diffraction spectrum in Figure 6. The Mo is still heterogeneously distributed in the matrix, which is evident from Mo enriched, full β phase regions, indicated by the white arrow. Due to the presence of the α phase, solute redistribution causes the β peaks to shift slightly to the right compared to the as built specimen. Furthermore, this also causes the microsegregation due to the cellular substructure to disappear. The extremely fine two phase microstructure leads to a higher hardness of $468 \pm 7 \text{ HV}_{0.3;10s}$, which is remarkably higher than that of the Ti6Al4V material processed via SLM ($399 \text{ HV}_{0.3;10s}$).

Micrographs of the sample treated at 850°C in Figure 5b show slightly etched regions at β grain boundaries and along the contours of the melt pools. The white arrow indicates the Mo enriched zones around the Mo particles, consisting fully of β phase. The α phase volume fraction is too small to cause any hardening. After heat treatment at 850 °C, the microhardness now equals $338 \pm 6 \text{ HV}_{0.3;10s}$, the same as in the as built condition (338 HV). The α peaks in the diffraction spectrum are almost invisible relative to the β phase peaks, but are still present under closer inspection, indicated in the diffraction spectrum in Figure 6.

At 900°C, there is almost no α phase left, as shown in Figure 5c. Additionally, α peaks in the diffraction spectrum in Figure 6 are indistinguishable from background noise. At $331 \pm 8 \text{ Hv}$, the hardness is again identical to that of the as built condition. Because of the limited amount of α phase present after quenching from 900°C, the β transus is likely located just above 900°C, corresponding well to the expected transus temperature.

After heat treatment at 1050°C, the microstructure is again fully β . The β grains did not grow significantly, and the hardness is $336 \pm 4 \text{ HV}_{0.3;10s}$.

3.2 Texture

Pole figures for the $\langle 100 \rangle$, $\langle 110 \rangle$ and $\langle 111 \rangle$ crystal orientations are given in Figure 7. The $\langle 100 \rangle$ direction is oriented preferentially in the building direction. This direction is known as the easy-growth direction for bcc crystals, as they grow quickest when the $\langle 100 \rangle$ crystal direction is aligned with the maximum temperature gradient [28]. However, the peak is slightly diffuse in the X-direction. The representation of the cubic crystal on the right illustrates the physical link between these pole figures. Specifically, the (001), (011) and $(\bar{1}11)$ directions are indicated.

3.3 Mechanical properties

Stress-strain curves for Ti6Al4V and Ti6Al4V+10Mo processed via SLM are shown in Figure 8. The lower Young's modulus of the fully β Ti6Al4V+10Mo is apparent from the more gradual slope of the elastic regime. The Young's modulus equals 73 ± 1 GPa, and is much lower than conventional Ti6Al4V which has a modulus of 105-120 GPa. Secondly, at an average of 20.1 ± 2.0 %, the elongation of Ti6Al4V+10Mo is much higher than that of Ti6Al4V, which is only 7.3 ± 1.1 %, even though both were produced using identical parameter sets. The trade-off for a higher elongation is a lower yield stress. Ti6Al4V+10Mo yields at 858 ± 16 MPa, while the stronger martensitic Ti6Al4V yields at 1110 ± 9 MPa. Furthermore, the stress-strain curve of Ti6Al4V+10Mo displays no strain hardening. On the contrary, a slight drop in strength just after yielding indicates delayed movement of dislocations, requiring extra stress to overcome the pinning effect of Mo in solid solution and of small Mo particles. The UTS is quickly reached after the onset of plastic deformation, after which a constant stress plateau extends up to failure.

The results are summarized in Table 1, and minimum values for three typical β Ti alloys are given as a reference, namely wrought Ti15Mo (ASTM F2066), Ti12Mo6Zr2Fe (ASTM F1813) and Ti15Mo5Zr3Al. Ti6Al4V+10Mo combines high strength with excellent ductility and has a low Young's modulus. Moreover, it meets the elongation requirements set for Ti15Mo and exceeds the strength requirements by several 100 MPa. In addition, it only just falls below the strength requirements for

Ti12Mo6Zr2Fe, but is considerably more ductile. The tensile properties are comparable mostly with Ti15Mo5Zr3Al, in which the UTS after solution treatment in the β field ranges between 900 and 1000 MPa, the Young's modulus about 80 GPa and elongation around 20% [29]. This alloy is mostly used in corrosive environments due to its high Mo content.

Yasa *et al.* [23] investigated the energy absorption during Charpy V-notch impact testing of Ti6Al4V specimens fabricated by SLM. The energy absorption was found to be independent of building direction and equaled 11.5 ± 0.5 J. Ti6Al4V+10Mo absorbed much less energy upon impact, at only 3.8 ± 0.1 J for horizontally built specimens and 1.4 ± 0.5 J for specimens built parallel to the vertical axis. The difference between both directions is the direction of crack growth. In the horizontal specimens, the crack front is parallel to the building direction, but crack growth is in the horizontal direction. For the vertical specimens, the crack grows in between the layers. The fracture surface of a representative horizontal sample is rougher than that of a representative vertical sample, as shown in Figure 9. This means that the crack path is deflected more in the horizontal sample, through which more energy is absorbed.

Strain rate during tensile testing is around $5 \times 10^{-3} \text{ s}^{-1}$, while the strain rate during Charpy V-notch impact testing is 10^2 to 10^3 s^{-1} . Additionally, in contrast to α' Ti6Al4V, β Ti6Al4V10Mo possesses a ductile to brittle transition. In general, the transition temperature generally lies above room temperature [30], leading to low energy absorption during Charpy impact testing.

4. Discussion

4.1 β phase

Alloying elements in titanium stabilize either the α phase or the β phase or have an indiscernible effect on the phase equilibrium. The combined effect of the β stabilizers can be described with the Mo equivalent, for which the formula is given in Equation (2) [24]. In Ti6Al4V, the β phase transforms to α' martensite during fast cooling. In agreement with literature [20, 24, 31, 32], the addition of 10

wt% Mo completely suppresses this transformation and the β phase is fully retained. The effect of Mo on the martensitic transformation is twofold: firstly, the critical cooling rate to retain β is decreased. Secondly and more importantly, by adding β stabilizers, the M_s temperature is lowered drastically. The different microstructures translate into different hardness values.

$$M_{o_{eq}} = 1.0Mo + 0.67V + 0.44W + 0.28Nb + 0.22Ta + \dots - 1.0Al[\text{wt}\%] \quad (2)$$

The applied energy density of the SLM process ($E = P/(v.h.t)$) is sufficient to fully melt the Ti6Al4V powder, which has a melting temperature of 1668°C. However, Mo has a melting temperature of 2623°C and the Mo particles only melt partially. Furthermore, the reflectance of Mo for a laser wavelength of 1.06 μm is equal to 0.69 compared to 0.55 for pure Ti, meaning it will absorb somewhat less of the laser radiation [33]. Both factors promote only partial melting of Mo and lead to the Mo particle - Ti matrix microstructure described above, seen in Figure 4.

4.2 Solidification structure

During SLM, the heat is extracted from the liquid melt pool to the previously consolidated layers and the substrate. For pure metals, this leads to the stabilization of the solidification front. For alloys, however, due to the solute redistribution, the liquid may become undercooled, which is known as constitutional undercooling. This leads to the destabilization of the solidification front and a transition from a planar to a cellular or dendritic solidification mode. This transition occurs when the thermal gradient in the liquid phase at the solidification front becomes lower than the critical gradient indicated in Equation (3). In this equation, the critical thermal gradient $\delta T/\delta x_{crit}$ is written as a function of the overall solute concentration C_0 , the solute diffusion coefficient D_L in the liquid phase, the solute partition coefficient k , the solidification growth rate R and the gradient of the equilibrium melting point $\delta T_L/\delta C$.

$$\frac{\delta T}{\delta x_{crit}} = - \frac{C_0}{D_L/R} \frac{(1-k)}{k} \frac{\delta T_L}{\delta C} \quad (3)$$

Planar solidification is rare for alloys and usually requires slow solidification. Consequently, it is remarkable that the planar front is stable in Ti6Al4V processed via SLM, even though it contains 10wt% alloying elements and solidification rates are extremely high. This is caused by the narrow solidification range T_L-T_S of Ti6Al4V of only 5°C. This range is linked to the partition coefficients, as a larger range usually leads to values of k further away from the ideal value of one. The limited extent of solute partitioning lowers the critical gradient, thereby favoring planar solidification.

Adding 10 wt% Mo to Ti6Al4V disturbs this equilibrium. Most importantly, it expands the solidification range to 17 °C, more than 3 times the value without Mo, as is clear from the pseudo-binary phase diagrams in Figure 10d-f and the calculated values in Table 2. The Mo itself has an average partition coefficient k_{Mo} of 1.41 over the whole solidification range. Furthermore, the calculations show that the increased solidification range decreases k_V to 0.33, less than half of its original value of 0.71. Additionally, Figure 10e shows that the effect of Al is reversed and the first solid to form will contain little Al, leading to an average k_{Al} of 0.27 over the whole solidification range. While Equation 3 has been analytically derived for a binary system, the impact of the different material parameters is similar in multi element alloys. The new partition coefficients of both Al and V lead to an increase of the second factor in Equation (3), thereby increasing the critical temperature gradient and promoting the destabilization of the solidification front.

The addition of an extra alloying element with a large partition coefficient additionally increases the critical gradient. A second effect of adding Mo is based on the relatively low diffusion coefficient of Mo in Ti. While reliable data for the diffusion coefficients of Al, V and Mo in liquid Ti is unavailable, the diffusion coefficient of Mo in β Ti is lower than that of Al and V [34]. This affects the first term, again increasing the critical gradient. These combined effects lead to instability of the planar solidification front and induce a cellular solidification. Figure 11 shows the transition from planar to cellular solidification at the melt pool boundary. The striped lines delineate the planar zone for the top melt pool. During the first stage of solidification, the concentration gradients at the liquid-solid

interface are still increasing and have not reached a steady state. Consequently, the critical thermal gradient for planar solidification is low and a planar front is stable. At a certain moment enough solute distribution will have taken place to increase the critical thermal gradient above the actual thermal gradient, at which point the solidification switches from a planar to a cellular mode. This transition can occur before a steady state is reached.

The change from planar to cellular solidification induces a change in microstructure. While large vertical columnar β grains were formed by the planar solidification of Ti6Al4V, cellular growth in Ti6Al4V+10Mo led to smaller elongated β grains oriented towards the center of the melt pool. This also has consequences on the texture that is developed. The dendrites grow primarily with the $\langle 100 \rangle$ direction along the heat flow direction, while texture development in planar solidification is mainly due to epitaxial growth of the crystals of the solid layers below.

In this research, the choice of Mo as additional alloying element was based on its ability to stabilize the β phase and its high melting temperature, which allowed retaining partially melted Mo particles in the Ti matrix. Additionally, it increases the corrosion resistance of Ti alloys. However, based on the specific requirements of certain applications, the alloy content can be tailored to induce a particular microstructure and meet required mechanical or physical properties. For instance, some regard the columnar prior β grains in Ti6Al4V as disadvantageous, because they lead to anisotropic properties. A different element that destabilizes the planar solidification front but does not affect the stability of the α or β phase can then be added, such as Zr.

On the other hand, changing the alloy content may facilitate easier processing via SLM while still maintaining the properties of the original alloy. In this sense, alloys that are prone to solidification cracking and thermal cracking can be alloyed or de-alloyed to increase toughness and eliminate cracks. Existing alloys were all designed to meet specific requirements, but also for a certain processing technique. Consequently, it is only logical that new alloy compositions are formulated to allow easy processing via SLM.

During simple, unidirectional cooling the rotation around the $\langle 100 \rangle$ direction is unrestricted and a fiber like texture appears which would result in pole figures with circular patterns. Instead, local peaks arise where the circle should have been. This is an artifact of the scanning strategy, which included a rotation of 90° between each layer. This fourfold symmetry of the scanning strategy is reflected in the presence of four local peaks in the $\langle 111 \rangle$ pole figure. This type of control of the texture via modification of the scanning strategy has previously been reported by Thijs *et al.* [35], and occurs both in Ti6Al4V and Ti6Al4V+10Mo. Furthermore, the central peak in the $\langle 100 \rangle$ pole figure is smeared in the X-direction. This is because of the local variations of the heat flow within the melt pool. The maximum temperature gradient is located perpendicular to the melt pool boundary, which has a concave shape. Grains grow from the boundary toward the center of the melt pool. This happens at an increasing angle relative to the building direction for grains starting higher near the surface of the melt. However, the top of a deposited layer is remolten during the application of the subsequent layer, thereby remelting all grains near the top of the previously solidified melt tracks. What remains is the bottom part of the previously solidified melt, where grains are more or less oriented parallel to the building direction. In the specific case, the cross-section was cut exposing more melt tracks in the Y-direction. The grains are then perpendicular to the sides of the melt tracks, in the X-direction, as is schematically shown in Figure 12.

5. Conclusion

10 wt% Mo powder was mixed with Ti6Al4V-ELI powder and processed via SLM, which led to a lower β transus temperature of around 900°C and the stabilization of the β phase at room temperature after rapid solidification. Moreover, the solidification mechanism changed from planar to cellular due to severe solute distribution between liquid and solid, which is a direct result of tripling the solidification temperature range. The resulting microstructure consists of homogeneously dispersed Mo particles in a fully β titanium matrix with a $\langle 100 \rangle$ cube texture in the building direction. In

addition, static tensile properties show a combination of high strength ($\sigma_{0.2}=858$ MPa) and excellent ductility ($\epsilon_{\text{frac}}=20.1$ %).

The presented results highlight the capabilities of SLM to process powder mixtures of different materials. This allows tailoring of the microstructure or producing material with superior properties. On the other hand, it can facilitate easier processing of certain materials via Additive Manufacturing, for instance by adding alloying elements that toughen the material and reduce problems with thermal stresses. Just as alloys were previously designed for other processing techniques such as casting or forging, purposeful formulation of alloys for Additive Manufacturing may greatly increase the AM material pallet.

Acknowledgements

Both B. Vrancken and L. Thijs would like to thank the Agency for Innovation by Science and Technology (IWT). The authors are grateful for the support of Dr. Shuigen Huang in performing the thermodynamic calculations. Partial financial support is also appreciated from KULeuven GOA/10/12.

References

- [1] Kruth JP, Levy G, Klocke F, Childs THC. CIRP Ann-Manuf. Technol. 2007;56:730.
- [2] Gu DD, Hagedorn YC, Meiners W, Meng GB, Batista RJS, Wissenbach K, Poprawe R. Acta Mater. 2012;60:3849.
- [3] Chlebus E, KuÅnicka Ba, Kurzynowski T, DybaÅ,a B. Mater. Charact. 2011;62:488.
- [4] Bormann T, Schumacher R, Muller B, Mertmann M, de Wild M. J. Mater. Eng. Perform. 2012;21:2519.
- [5] Meier H, Haberland C, Frenzel J, Zarnetta R. Selective Laser Melting of NiTi shape memory components. Boca Raton: Crc Press-Taylor & Francis Group, 2010.
- [6] Zhang LC, Klemm D, Eckert J, Hao YL, Sercombe TB. Scripta Mater. 2011;65:21.
- [7] Das S, Wohler M, Beaman JJ, Bourell DL. Materials & Design 1999;20:115.

- [8] Thijs L, Verhaeghe F, Craeghs T, Van Humbeeck J, Kruth JP. *Acta Mater.* 2010;58:3303.
- [9] Murr LE, Quinones SA, Gaytan SM, Lopez MI, Rodela A, Martinez EY, Hernandez DH, Martinez E, Medina F, Wicker RB. *Journal of the Mechanical Behavior of Biomedical Materials* 2009;2:20.
- [10] Facchini L, Magalini E, Robotti P, Molinari A, Hoges S, Wissenbach K. *Rapid Prototyping J.* 2010;16:450
- [11] Vilaro T, Colin C, Bartout JD. *Metall. Mater. Trans. A* 2011;42A:3190.
- [12] Vrancken B, Thijs L, Kruth J-P, Van Humbeeck J. *J. Alloys Compd.* 2012;541:177.
- [13] Hua T, Jing C, Fengying Z, Xin L, Weidong H. *Rare Metal Materials and Engineering* 2009;38:574.
- [14] Gu D, Hagedorn Y-C, Meiners W, Wissenbach K, Poprawe R. *Surf. Coat. Technol.* 2011;205:3285.
- [15] Gu D, Meiners W. *Materials Science and Engineering: A* 2010;527:7585.
- [16] Gu DD, Meng GB, Li C, Meiners W, Poprawe R. *Scripta Mater.* 2012;67:185.
- [17] Banerjee R, Bhattacharyya D, Collins PC, Viswanathan GB, Fraser HL. *Acta Mater.* 2004;52:377.
- [18] Banerjee R, Collins PC, Genç A, Fraser HL. *Materials Science and Engineering: A* 2003;358:343.
- [19] Collins PC, Banerjee R, Banerjee S, Fraser HL. *Materials Science and Engineering: A* 2003;352:118.
- [20] Almeida A, Gupta D, Loable C, Vilar R. *Materials Science and Engineering: C* 2012;32:1190.
- [21] Van Vaerenbergh J. *Process optimisation in Selective Laser Melting.* vol. PhD. Twente: University of Twente, 2008.
- [22] Van Hooreweder B, Moens D, Boonen R, Kruth J-P, Sas P. *Adv. Eng. Mater.* 2012;14:92.
- [23] Yasa E, Deckers J, Kruth JP, Rombouts M, Luyten J. *Virtual Phys. Prototyping* 2010;5:89.
- [24] Collings E. *American Society for Metals*, 1984 1984:261.
- [25] Vrancken B, Wauthlé R, Kruth JP, Van Humbeeck J. *Proceedings of the Solid Freeform Fabrication Symposium* 2013:393.

- [26] Thijs L, Kempen K, Kruth J-P, Van Humbeeck J. Acta Mater. 2013.
- [27] Murray JL. Bulletin of Alloy Phase Diagrams 1981;2:185.
- [28] Messler RW. Principles of Welding: Wiley, 2008.
- [29] Boyer RR, Welsh G, Collings EW. Materials properties handbook: Titanium alloys: ASM International, Materials Park: Ohio, 1994.
- [30] Lederich RJ, Schwartz DS, Sastry SML. Beta Titanium Alloys in the 1990s. Warrendale: Minerals, Metals & Materials Soc, 1993. p.159.
- [31] Bania P. JOM 1994;46:16.
- [32] Ho WF, Ju CP, Chern Lin JH. Biomaterials 1999;20:2115.
- [33] Palik ED. Handbook of Optical Constants of Solids, Volumes I, II, and III: Subject Index and Contributor Index: Elsevier Science & Tech, 1985.
- [34] Zwicker U. Selbstdiffusion und Diffusion von Fremdatomen. Titan und Titanlegierungen, vol. 21. Springer Berlin Heidelberg, 1974. p.102.
- [35] Thijs L, Vrancken B, Kruth JP, Van Humbeeck J. Proceedings of the Materials Science and Technology (MS&T) Conference 2013:21.

Figure Captions

Figure 1 Ti6Al4V+10Mo powder mixture. The large, spherical particles are Ti6Al4V. The irregular shaped, bright particles are Mo.

Figure 2 Side view cross section of the difference in macrostructure of A) Ti6Al4V and B) Ti6Al4V+10Mo processed by SLM. The white arrows indicate Mo particles. The same etchant was used to reveal both microstructures.

Figure 3 BSE image of the top surface, showing compositional differences in the matrix due to rapid solidification and the low diffusion coefficient of Mo. The white particles are unmolten Mo dispersed randomly in the matrix.

Figure 4 Side view of Ti6Al4V, taken with SE contrast in SEM. The arrows indicate locations where grains grew across the melt pool boundary. The two distinct white spots in the upper right corner are Mo particles and Mo enriched zones around the particles.

Figure 5 Side views of the microstructure of Ti6Al4V+10Mo after heat treatment. A) Fine $\alpha+\beta$ structure after heat treatment at 650°C. B) α phase is present in bands and at the β grain boundaries after quenching from 850°C. C) Almost no α phase is present after quenching from 900°C. The white arrows indicate Mo rich zones in which the β phase is fully stabilized. Notice the different scale of A compared to B and C.

Figure 6 Diffraction spectra for as built SLM Ti6Al4V+10Mo, and after heat treatment at 650°C, 850°C, 900°C and 1050°C. α peaks are clearly visible after heat treatment at 650°C, but are also present after heat treatment at 850°C, as illustrated by the close ups in the diffraction spectrum.

Figure 7 Pole figures illustrating the $\langle 100 \rangle$ texture. The building direction is out of plane in the Z direction.

Figure 8 Engineering stress-Strain curves for Ti6Al4V and Ti6Al4V10Mo, as produced by SLM.

Figure 9 Fracture surfaces of Charpy V-notch specimens. The white arrows indicate the crack propagation direction. The insert in the middle shows where the images were taken on the fracture surface, and the orientation of the fracture surfaces with respect to the layers.

Figure 10 Calculated vertical pseudo-binary phase diagrams of the different phase diagrams. A) General representation of the partition coefficient k for solute X. B) Ti6Al4V system with varying amount of Al. C) Ti6Al4V system with varying amount of V. D) Ti6Al4V10Mo system with varying amount of Mo. E) Ti6Al4V10Mo system with varying amount of Al. F) Ti6Al4V10Mo system with varying amount of V.

Figure 11 Thin region at the melt pool boundary in which planar solidification is stable. Transition from planar to cellular solidification occurs within 0.5 to 1 μm of the melt pool boundary.

Figure 12 Partial remelting of underlying layers removes horizontally grown grains at the top of the melt pools. This results in the smearing effect of the <100> texture. The red arrows indicate the approximate orientation of the <100> direction within the individual grains.

Table Captions

Table 1 Static tensile properties of Ti6Al4V + 10Mo compared to regular Ti6Al4V processed by SLM. For reference, standard specifications for two types of β titanium alloys for use in surgical implants are given as well as mechanical properties for Ti15Mo5Zr3Al. (*) Bar, beta annealed (**) Solution treated

Table 2 The solidification range ΔT and partition coefficient k for the different pseudo-binary sections of Ti6Al4V and Ti6Al4V10Mo, as calculated by ThermoCalc. The partition coefficient is an average value over the whole solidification range.

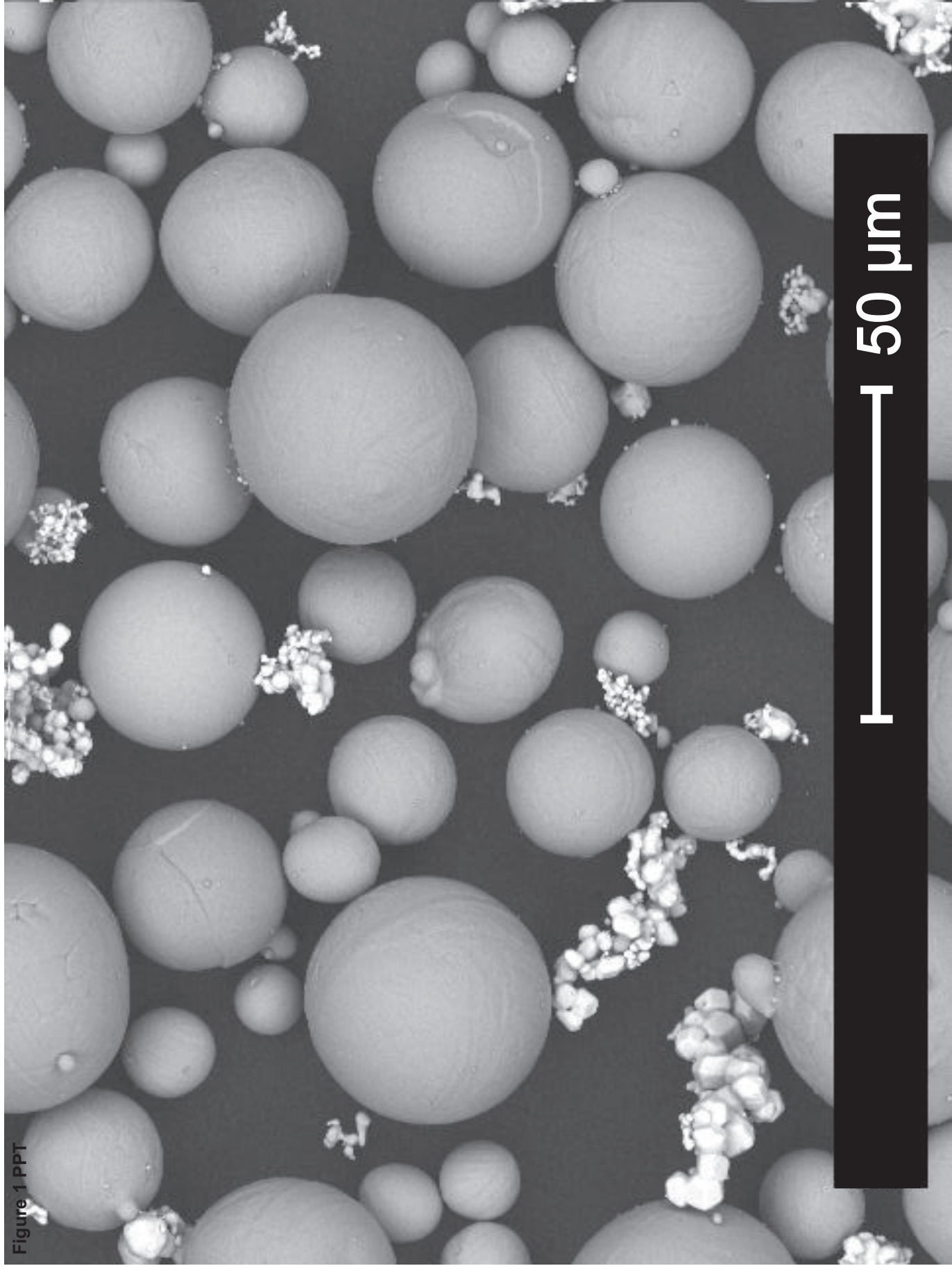


Figure 1 PPT

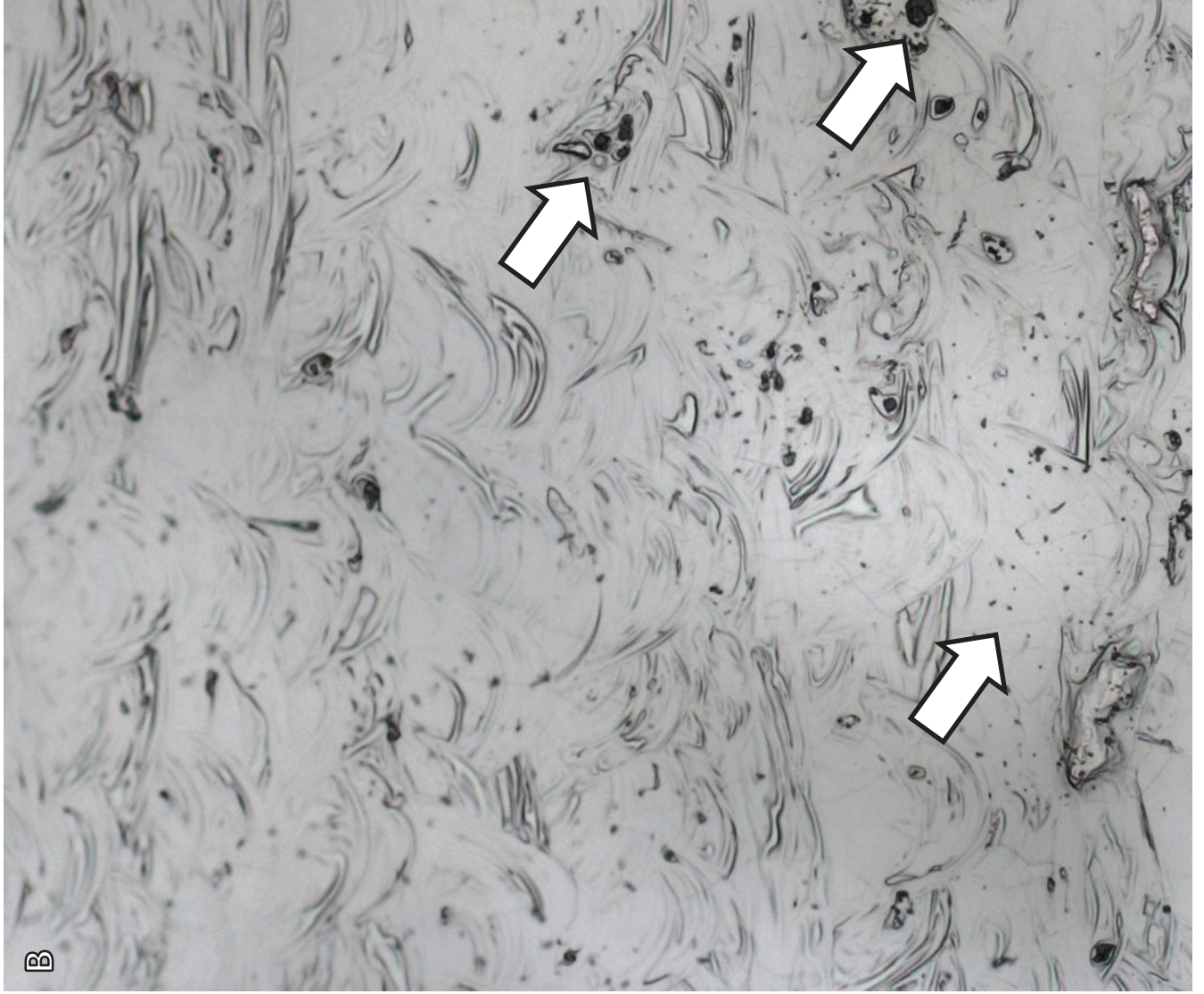
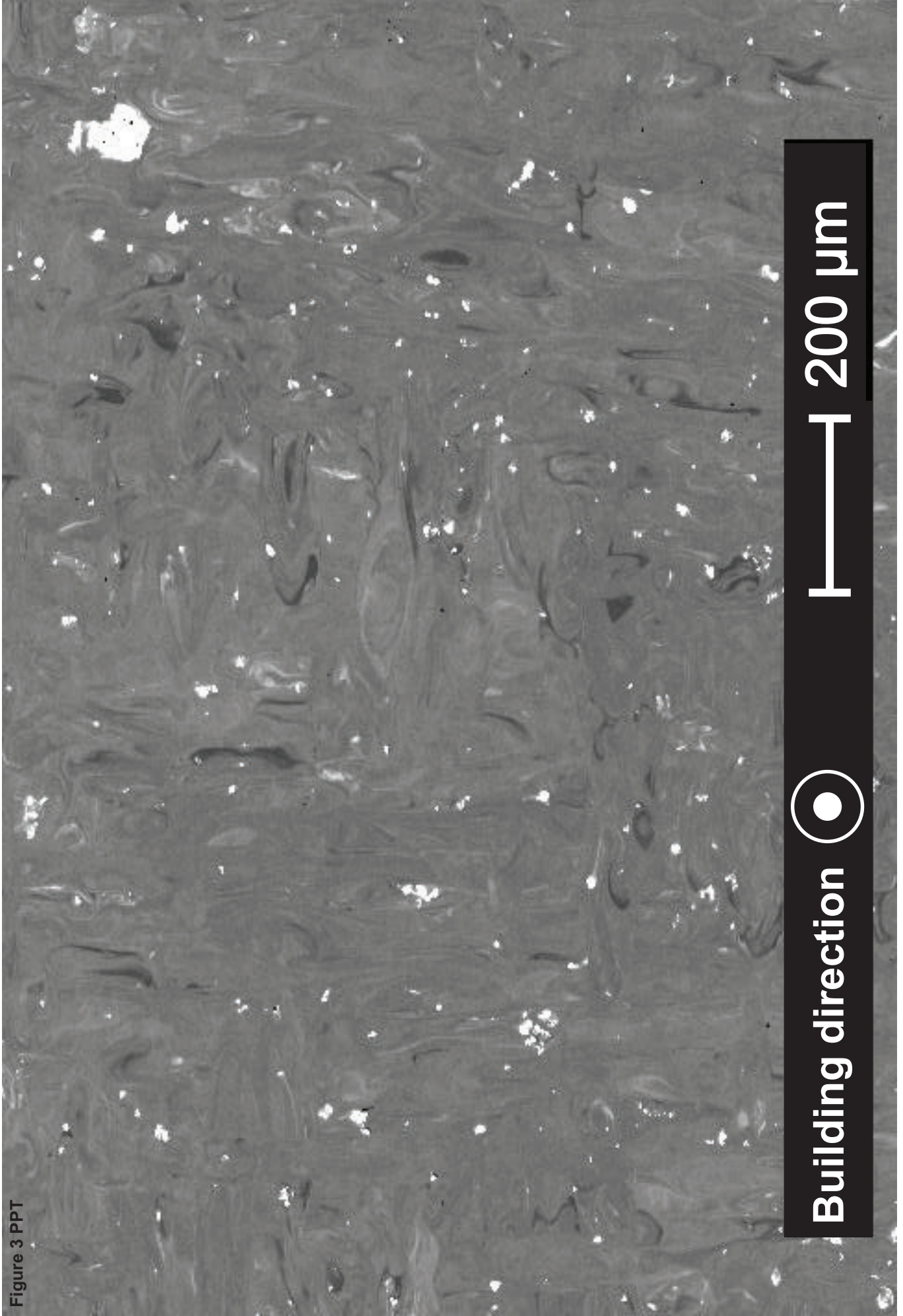
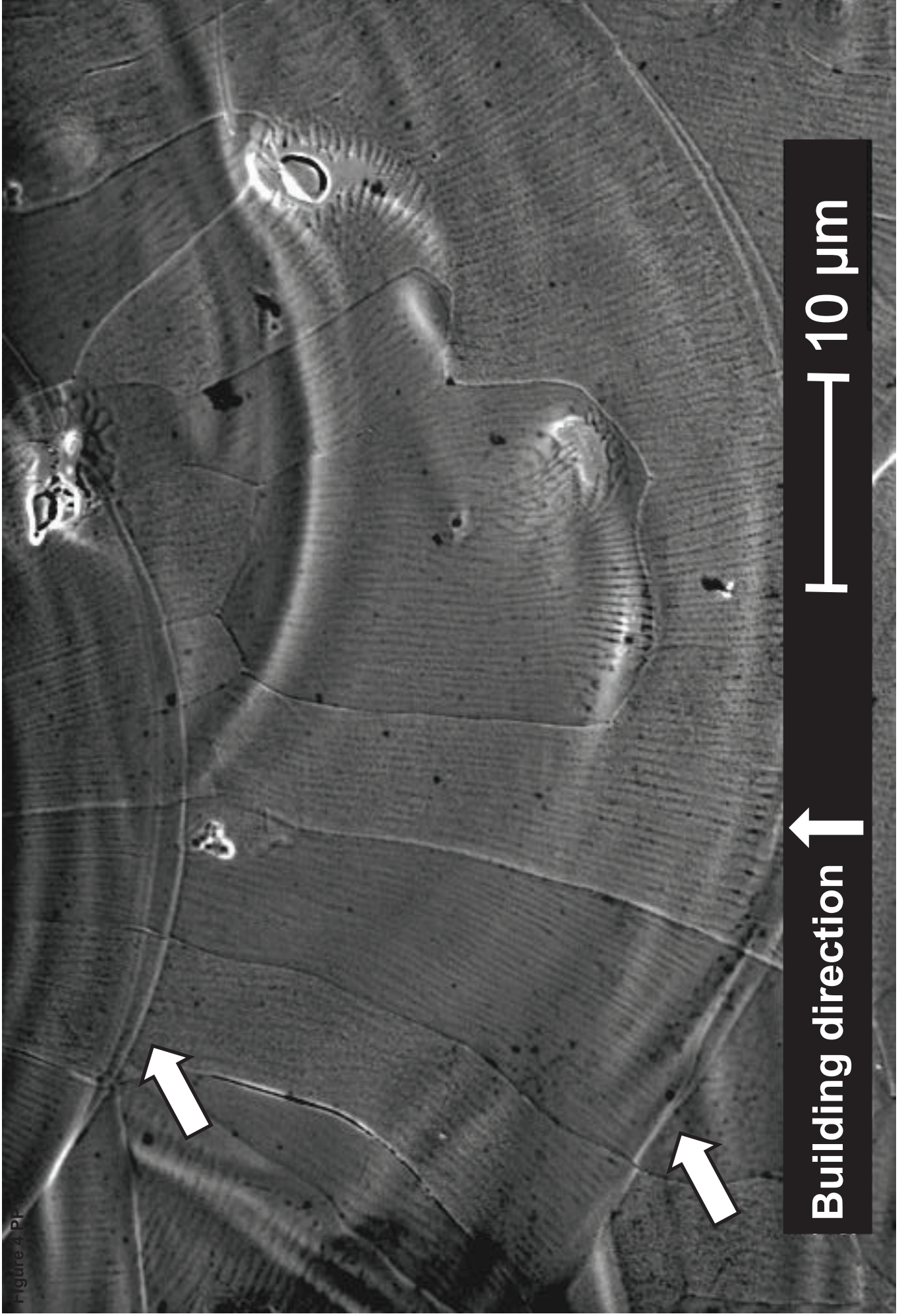


Figure 3 PPT



Building direction

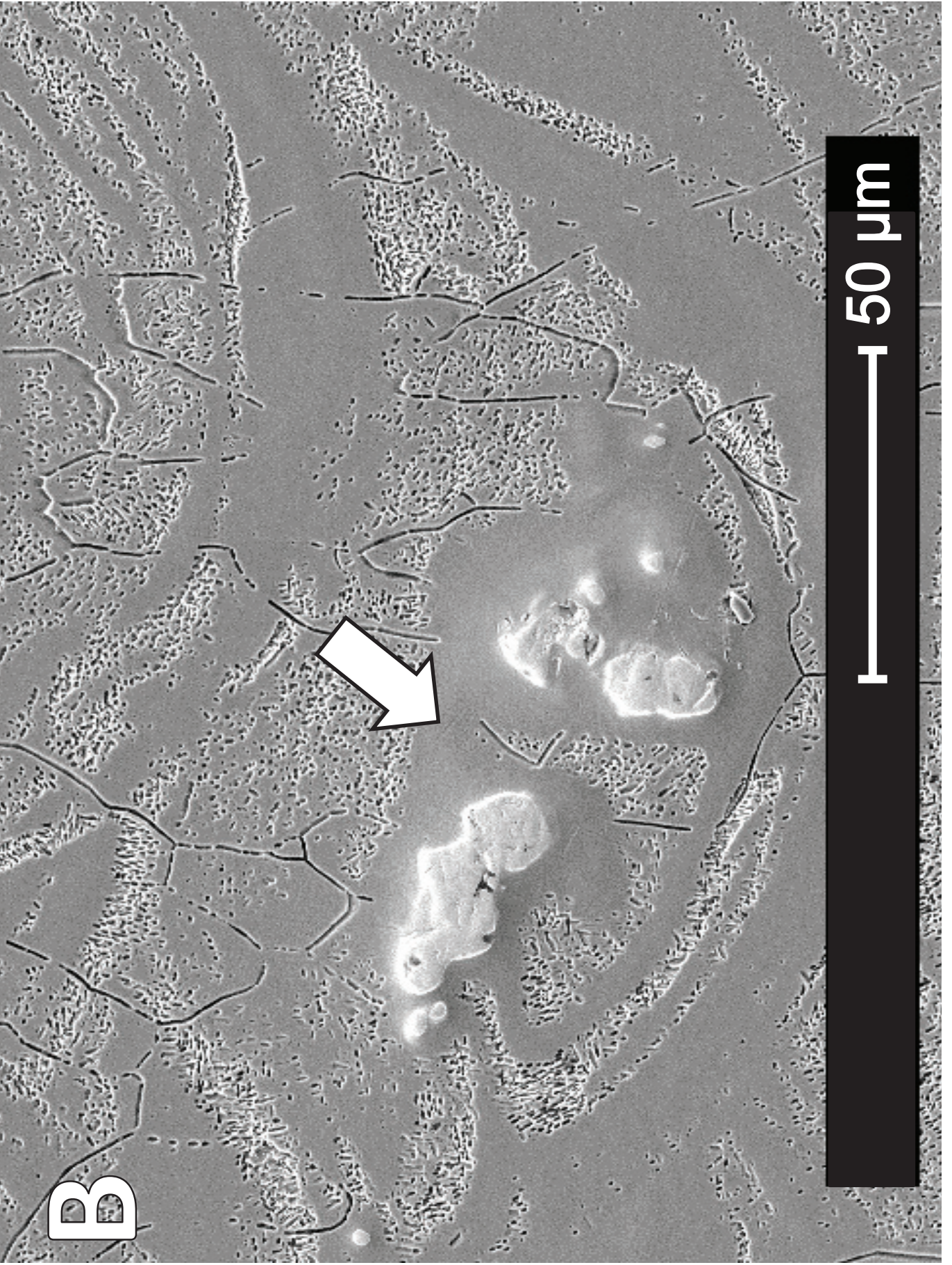
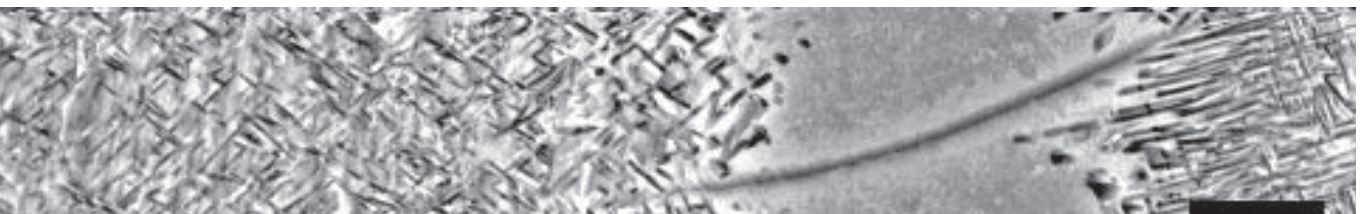
200 μm



10 μm

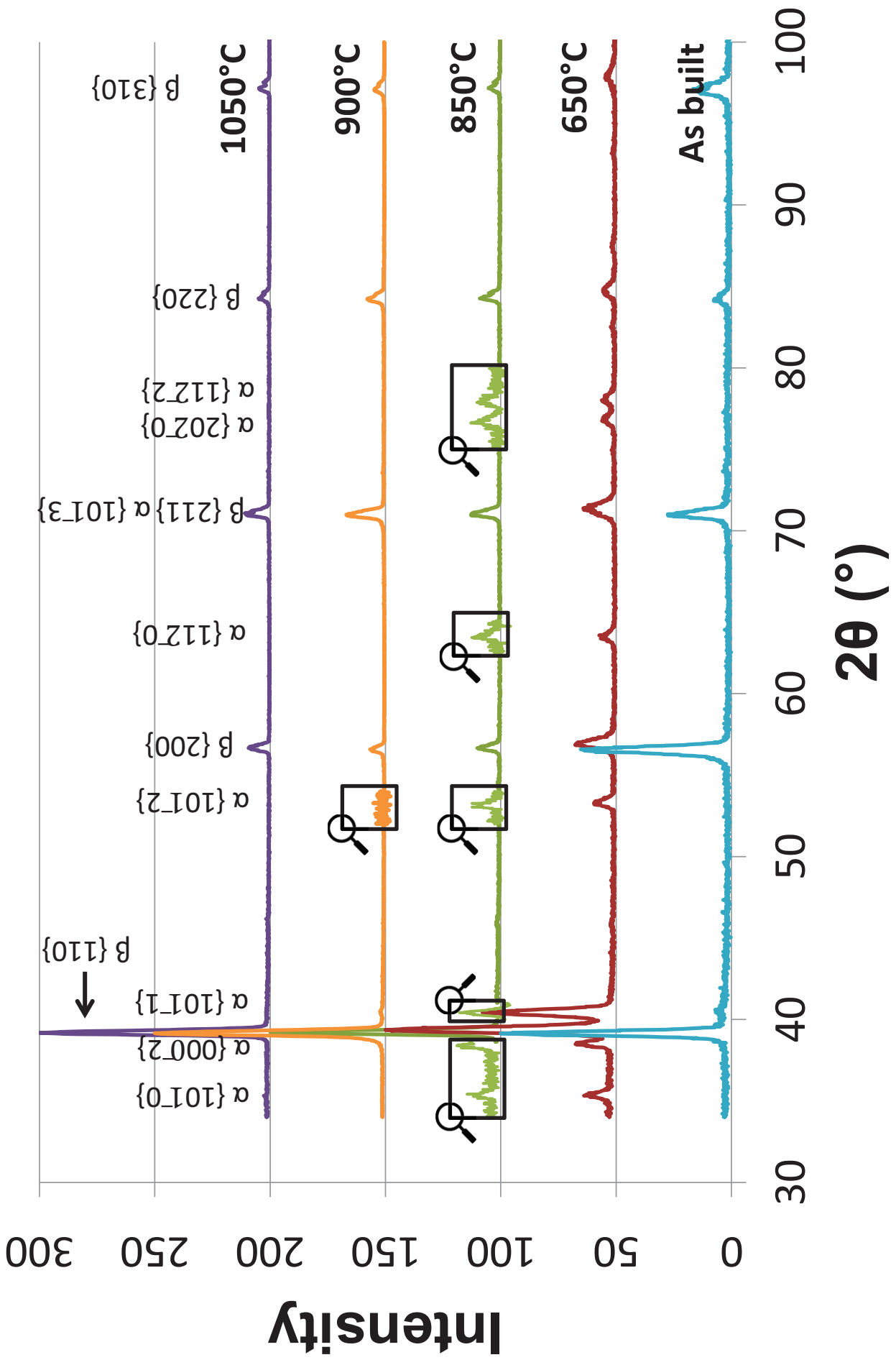
Building direction \uparrow

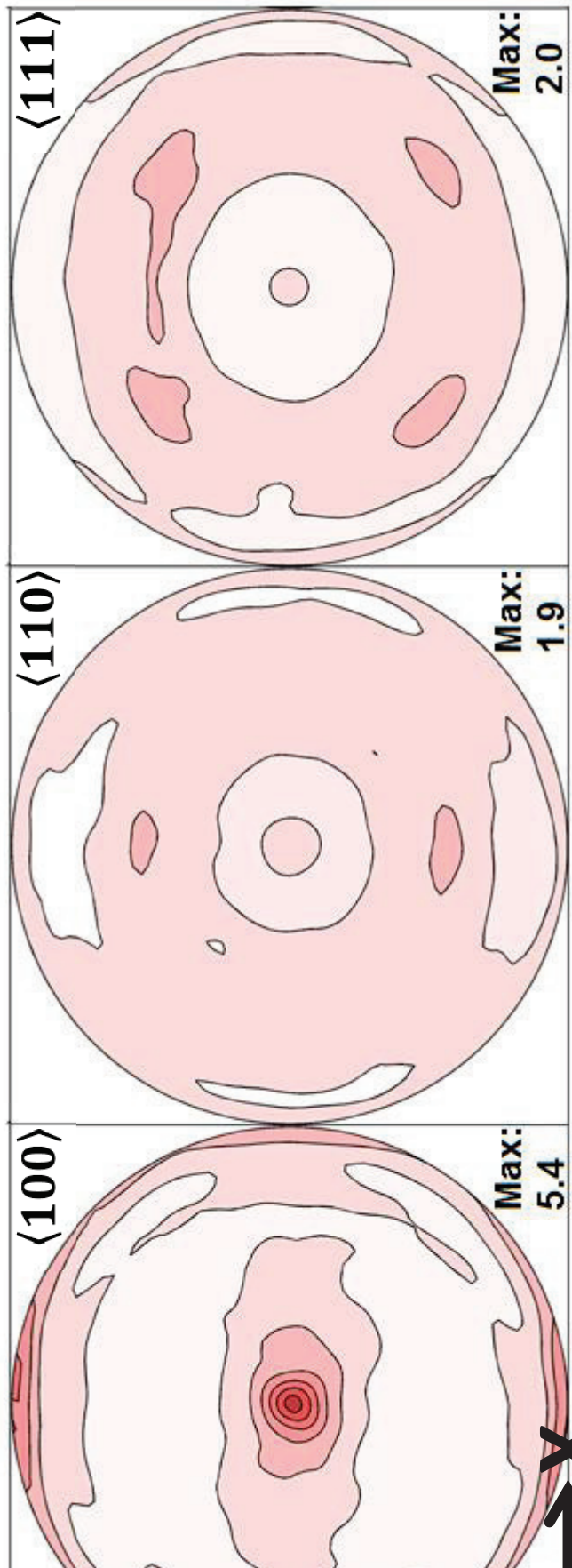
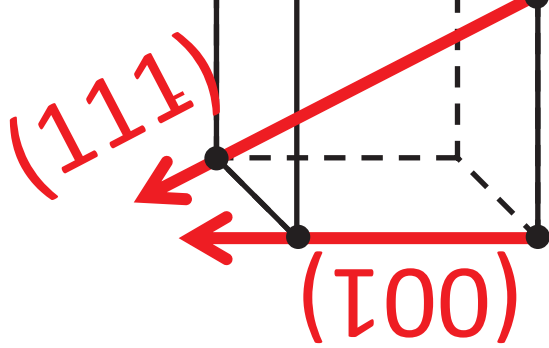
Figure 4 PF

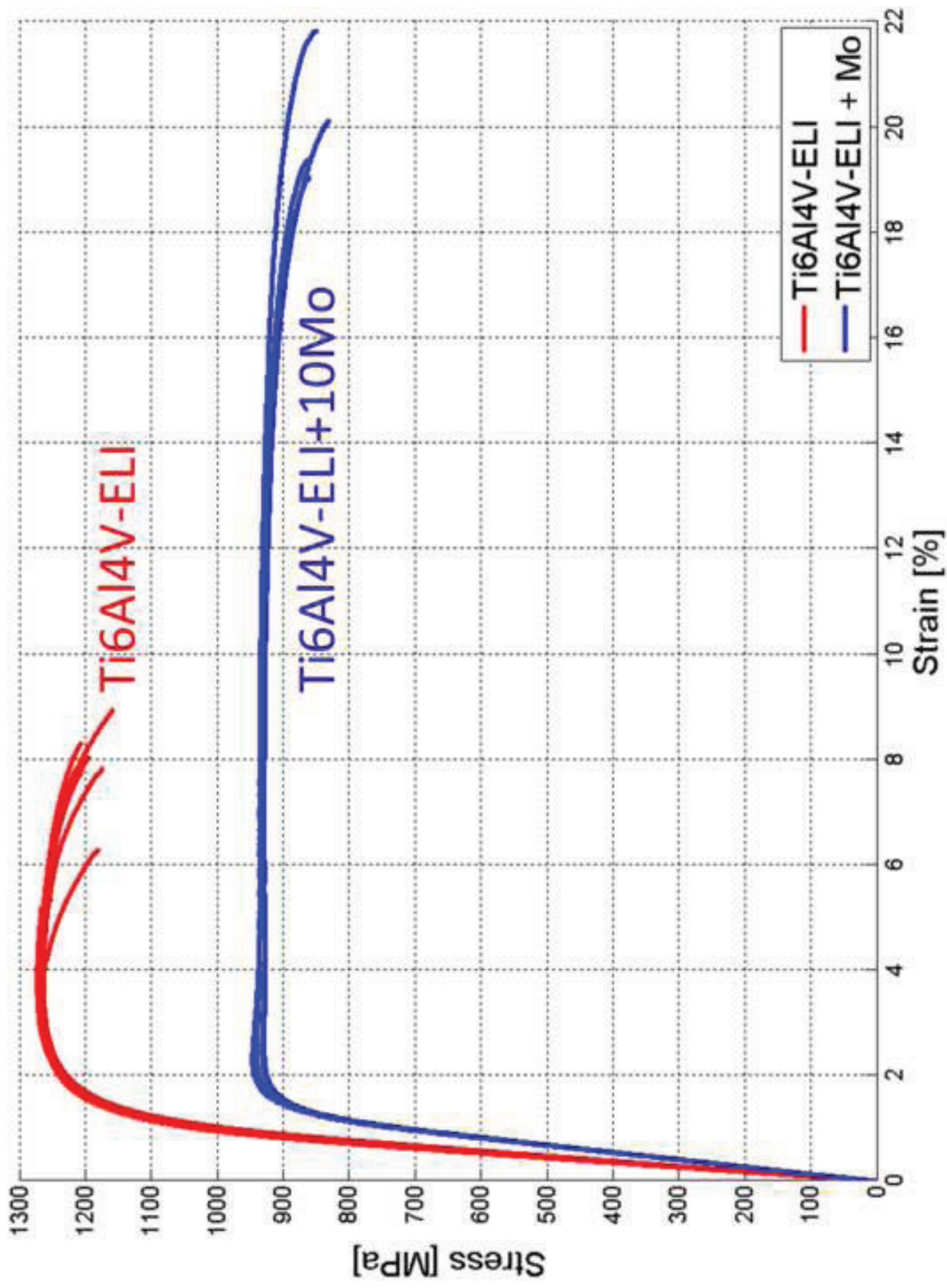


B

C

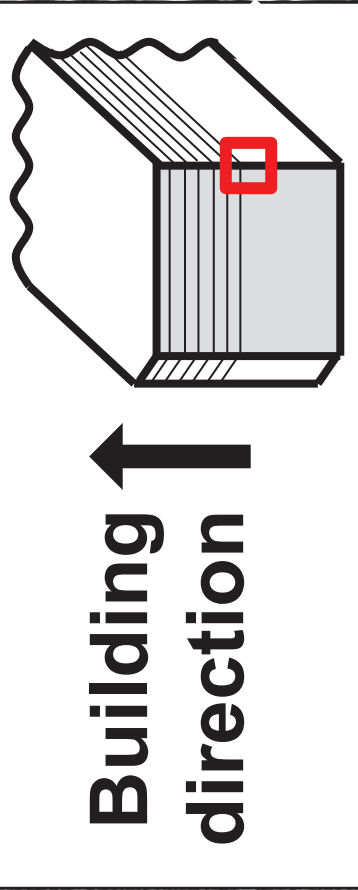




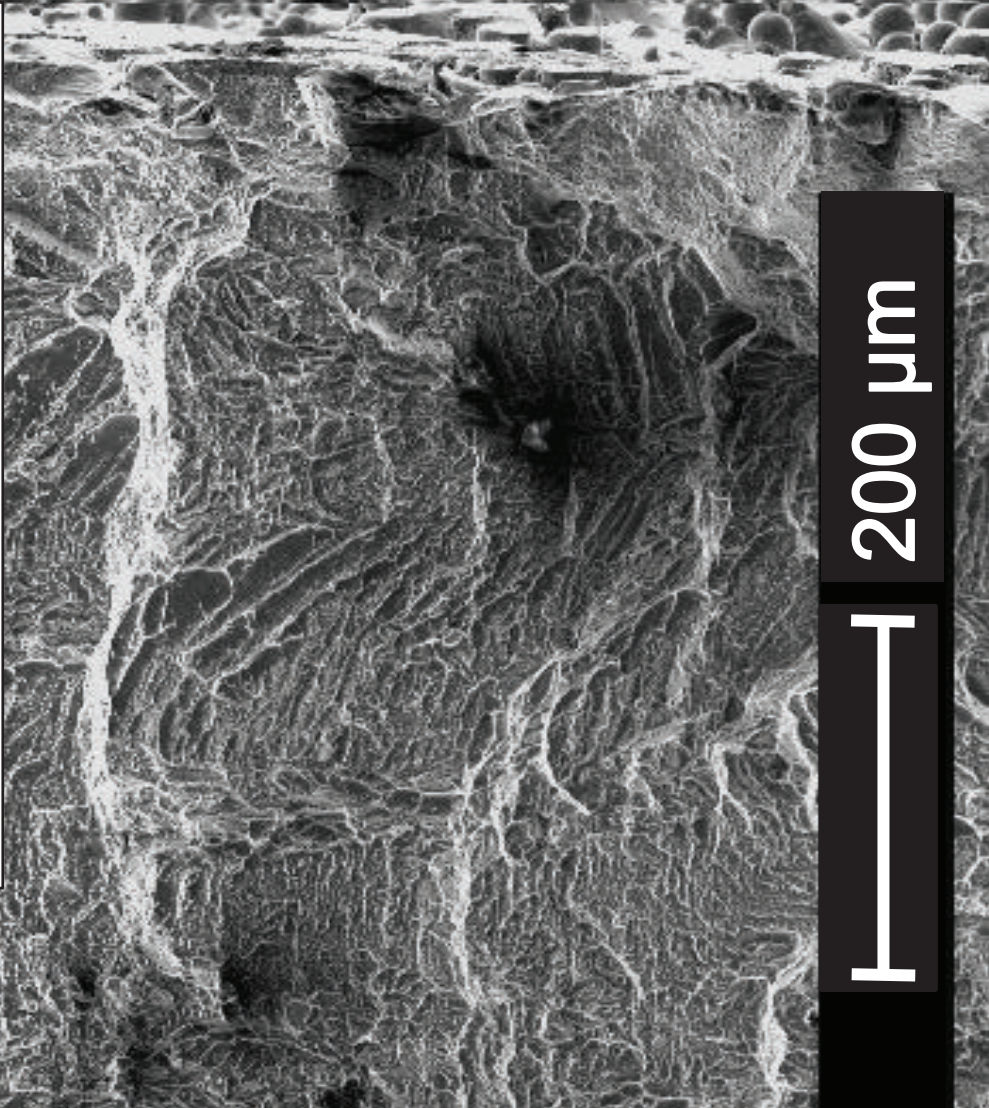


**Bu
dire**

B

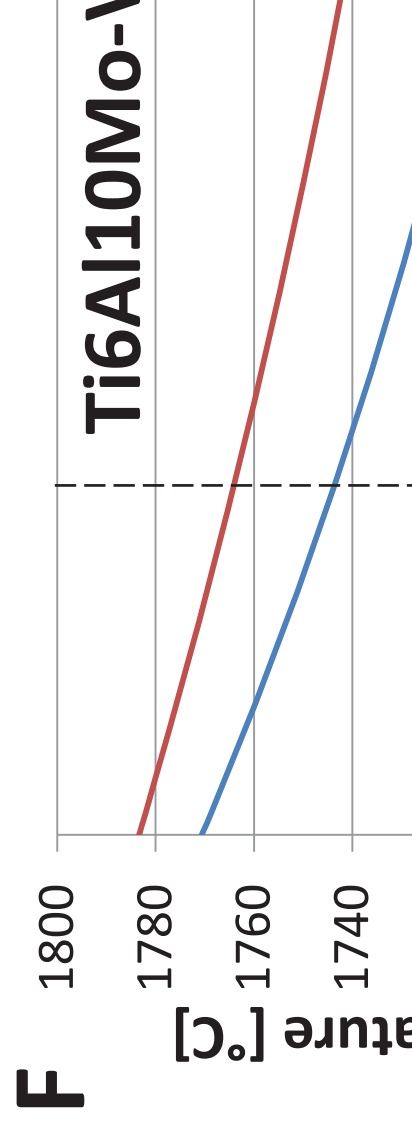
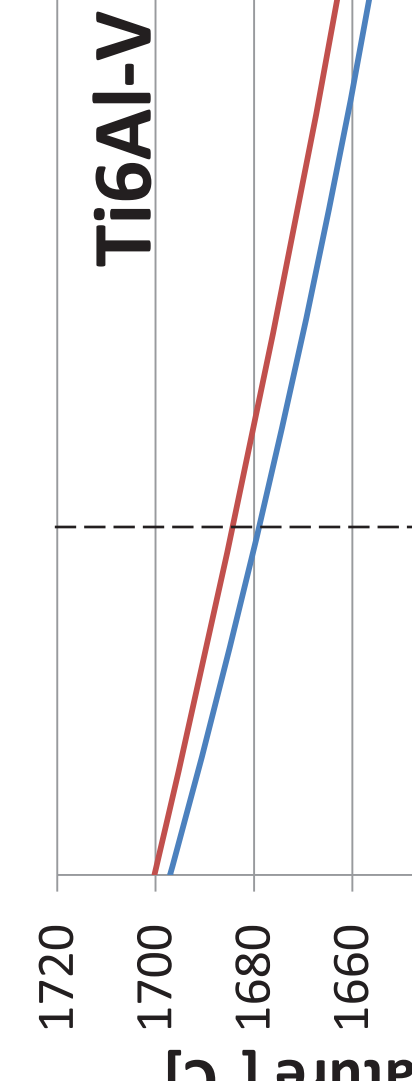
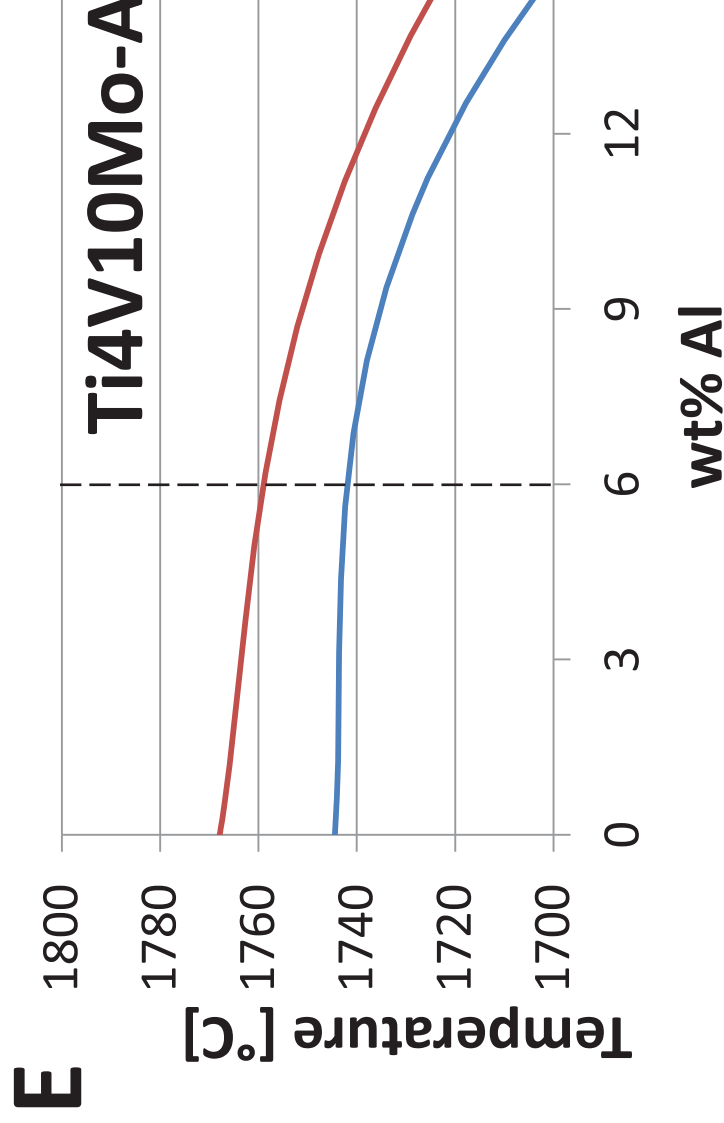
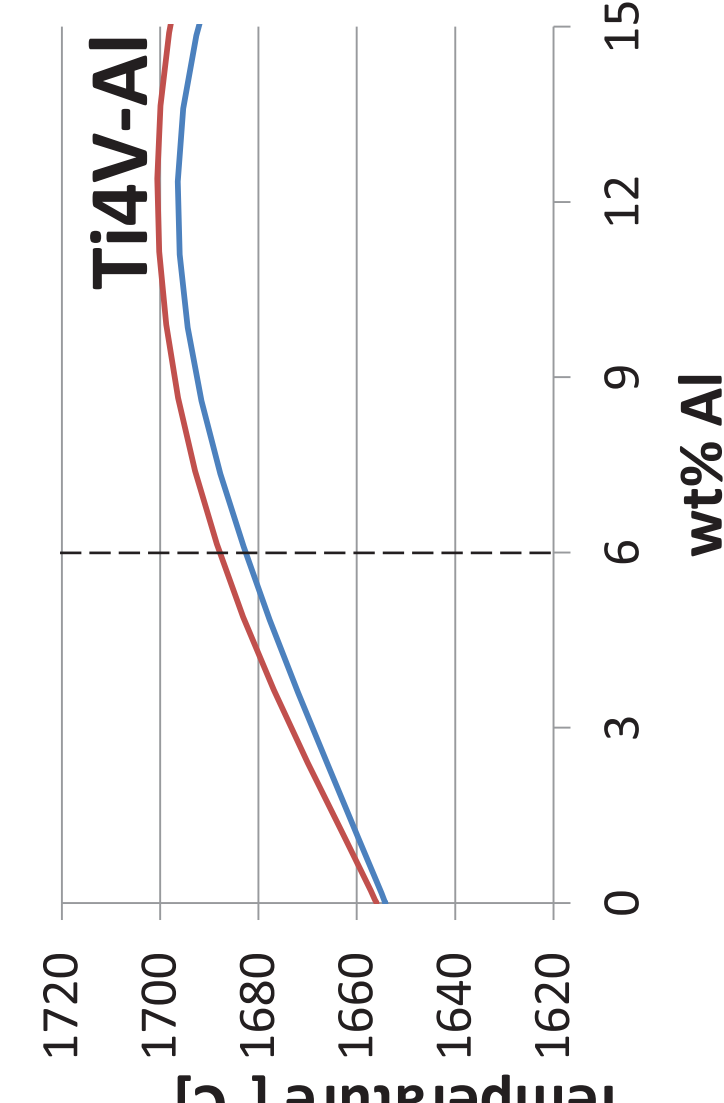
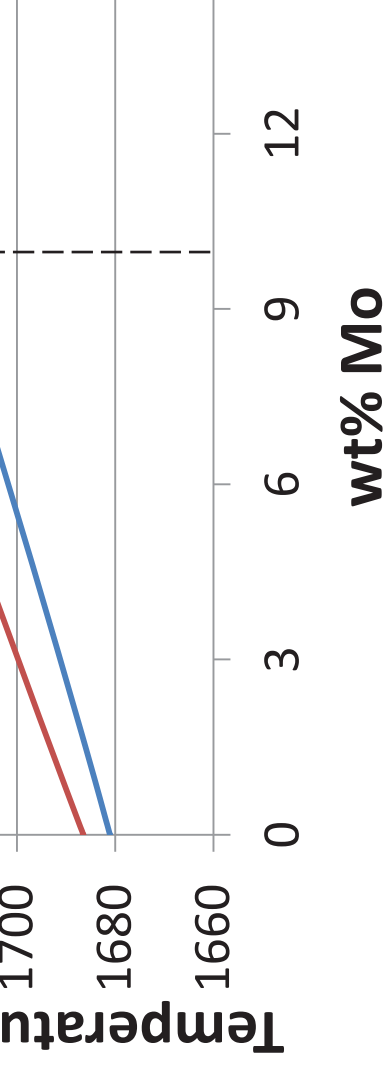
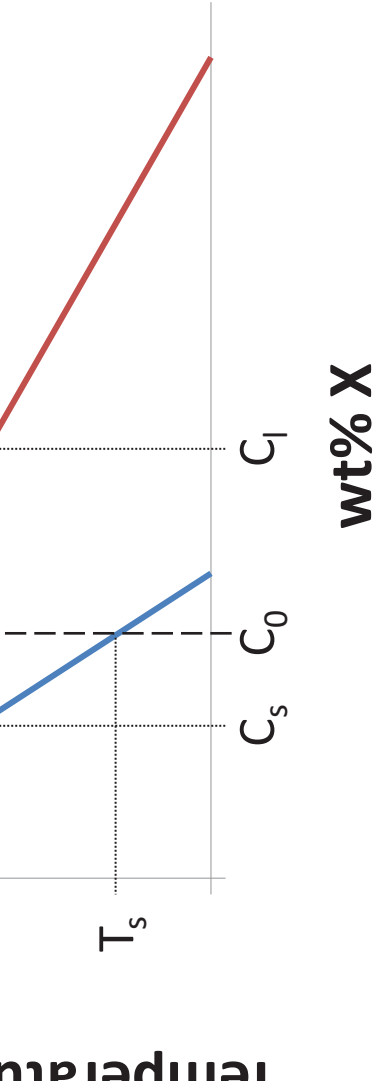


**Building
direction**



200 μ m





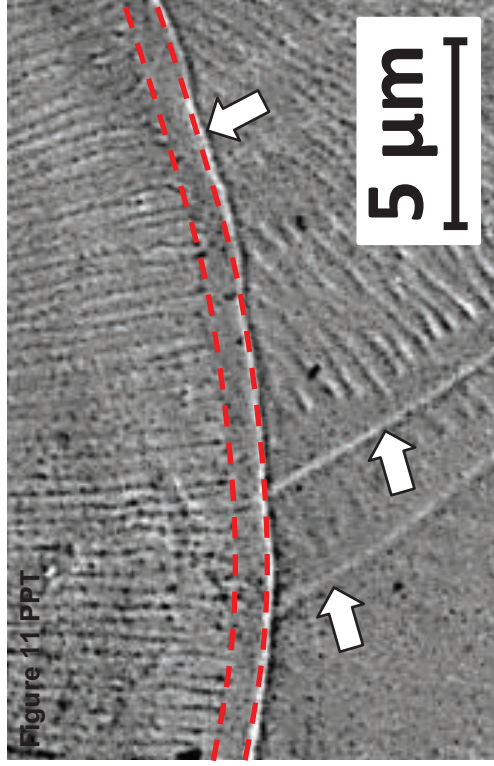


Figure 11 PPT

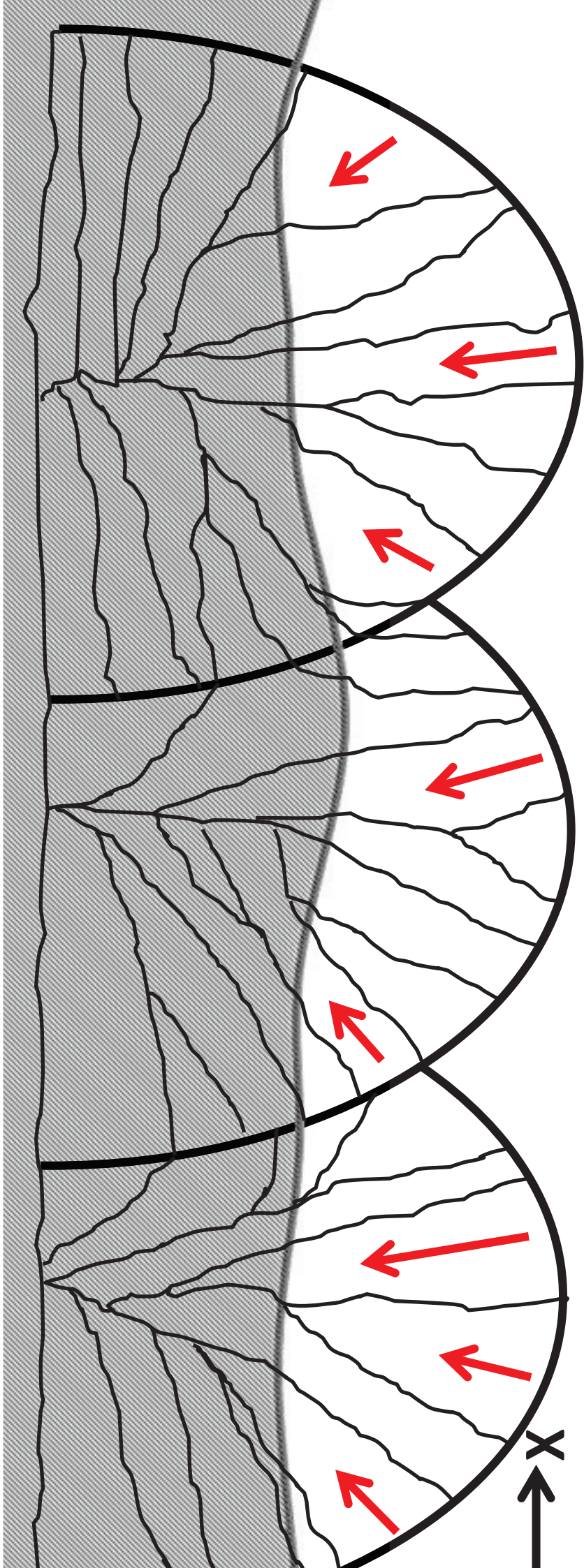


Table 1

	Young's modulus	Yield Stress	UTS	Fracture strain	Source
	E [GPa]	$\sigma_{0,2}$ [MPa]	σ_{max} [MPa]	ϵ_{max} [%]	
Ti6Al4V+10Mo	73 ± 1	858 ± 16	919 ± 10	$20,1 \pm 2,0$	
Ti6Al4V	109 ± 3	1110 ± 9	1267 ± 5	$7,3 \pm 1,1$	[12]
Ti15Mo	<i>Not given</i>	483	690	20	ASTM F2066*
Ti12Mo6Zr2Fe	<i>Not given</i>	897	932	12	ASTM F1813**
Ti15Mo5Zr3Al	80	<i>Not given</i>	900-1000	20	[29]

Table 2

		Ti6Al4V			Ti6Al4V10Mo	
		<i>Ti4V-xAl</i>	<i>Ti6Al-xV</i>	<i>Ti4V10Mo-xAl</i>	<i>Ti6Al10Mo-xV</i>	<i>Ti6Al4V-xMo</i>
ΔT [°C]		5			17	
k		1.24	0.71	0.27	0.33	1.41